



Large-scale shaking table model test on seismic performance of bridge-pile-foundation slope with anti-sliding piles: a case study

Chonglei Zhang^{1,2} · Guanlu Jiang³ · Lijun Su^{1,2} · Da Lei³ · Weiming Liu¹ · Zhimeng Wang⁴

Received: 29 January 2019 / Accepted: 19 September 2019 / Published online: 5 November 2019
© Springer-Verlag GmbH Germany, part of Springer Nature 2019

Abstract

This study aimed to illustrate the seismic performances of anti-slide pile-reinforced bridge foundations in landslides. Based on the anti-slide reinforcement project at Yousuotun along the Chengdu-Lanzhou high-speed railway under construction, shaking table tests were performed on a double-row anti-slide pile-reinforced bridge foundation and landslide model with a 1:40 similitude ratio. Given that the similitude law was satisfied, seismic waves with different frequencies and acceleration amplitudes were input as base excitations to monitor the responses of dynamic parameters: slope acceleration, earth pressure, and pile strain. The amplification effect of peak ground acceleration (PGA) was analyzed. The landslide thrust distribution characteristics and slope response processes were further studied to verify the seismic design of such bridge foundations in landslide-prone areas. The response acceleration of the slope subjected to seismic loads showed a nonlinear amplification “elevation effect”, “surface effect”, and “geological structure effect”. When the distance between the bridge foundation and the back-row anti-slide pile was small, the pier maintained a relatively large PGA amplification factor and was subjected to strong seismic loads. The landslide thrust was mainly borne by the upper part of the back-row anti-slide piles as its distribution changed from spoon-shaped to bow-shaped. Under high-intensity earthquake events, the load-bearing section of the bridge foundation should be strengthened at the sliding surface. Anti-slide piles can effectively limit the dynamic response of the landslide and weaken the seismic response of the slope. The results of testing this reinforcement are the first results proving that the seismic design of reinforced bridge foundations with anti-slide piles can be reliable.

Keywords Anti-slide piles · Shaking table model · Peak ground acceleration · Bridge pile foundation · Seismic response

Introduction

Since the occurrence of the May 12 Wenchuan Ms 8.0 earthquake along the Longmenshan fault in 2008, southwestern China has experienced a number of earthquakes of medium

to high intensities (Ms 6.5–7.1) (Huang et al. 2017). Earthquake-induced landslides (co-seismic landslides) are often followed by devastating consequences (Cui et al. 2009; Xu et al. 2009; Wang et al. 2009). Co-seismic landslides, with higher kinematic velocities and longer run-out distances than

✉ Guanlu Jiang
wgljiang@home.swjtu.edu.cn

Chonglei Zhang
zhangchonglei@imde.ac.cn

Lijun Su
sulijun1976@163.com

Da Lei
china722309220@sina.cn

Weiming Liu
liuwm@imde.ac.cn

Zhimeng Wang
shandisuo@163.com

¹ Key Laboratory of Mountain Hazards and Earth Surface Processes, Institute of Mountain Hazards and Environment, Chinese Academy of Sciences, Chengdu 610041, China

² CAS Center for Excellence in Tibetan Plateau Earth Sciences, Beijing 100101, China

³ MOE Key Laboratory of High-speed Railway Engineering, School of Civil Engineering, Southwest Jiaotong University, Chengdu 610031, China

⁴ China Railway Eryuan Engineering Group Co. Ltd, Chengdu 610031, China

creep landslides (Pastor et al. 2009), have become one of the major geological disasters associated with earthquakes (Chigira et al. 2010; Gorum et al. 2011; Wasowski et al. 2011). The Chengdu-Lanzhou high-speed railway (Chenglan HSR) is one of the large transportation projects under construction in the alpine valley area on the eastern edge of the Qinghai-Tibet Plateau, which is an area with active neotectonics (Hubbard and Shaw 2009), as shown in Fig. 1. The topographic and geological conditions along the Chenglan HSR are characterized by the typical “three high characteristics” of high ground stress, high seismic intensity, and high geological hazard risk (Du et al. 2012). The difficult geologic conditions have complicated the slope-retaining measured used in this region (Huang et al. 2013). The Chenglan HSR includes a considerable number of piers in unfavourable slopes. The slopes are steep, generally steeper than 40° , and their reliefs range from 50 to 400 m. The bridge

foundation on a high steep slope is usually thrust horizontally by geological bodies. Due to the limited deformation requirements of a bridge foundation, the horizontal deformation of a pier must be less than $5\sqrt{L}$ (Kowalsky 2000; Hwang et al. 2000; Lee et al. 2005; TB10002.5-2005 2005; JGJ94- 2008 2008), where L is the bridge span. Under the action of high-intensity earthquakes, these high and steep slopes are prone to overall slip. To ensure the structural stability of the bridge foundation under seismic effects, carrying out anti-slide reinforcement for potential landslides and simultaneously considering the restrictions on the deformation of the pier foundation are necessary (Li et al. 2008; Han et al. 2009).

The co-seismic responses of natural high and steep slopes, such as the spatiotemporal responses in slope acceleration and dynamic stress, are receiving increasing academic attention (Chotesuwan et al. 2012). To mitigate natural disasters in mountainous areas, anti-slide piles are widely used to control

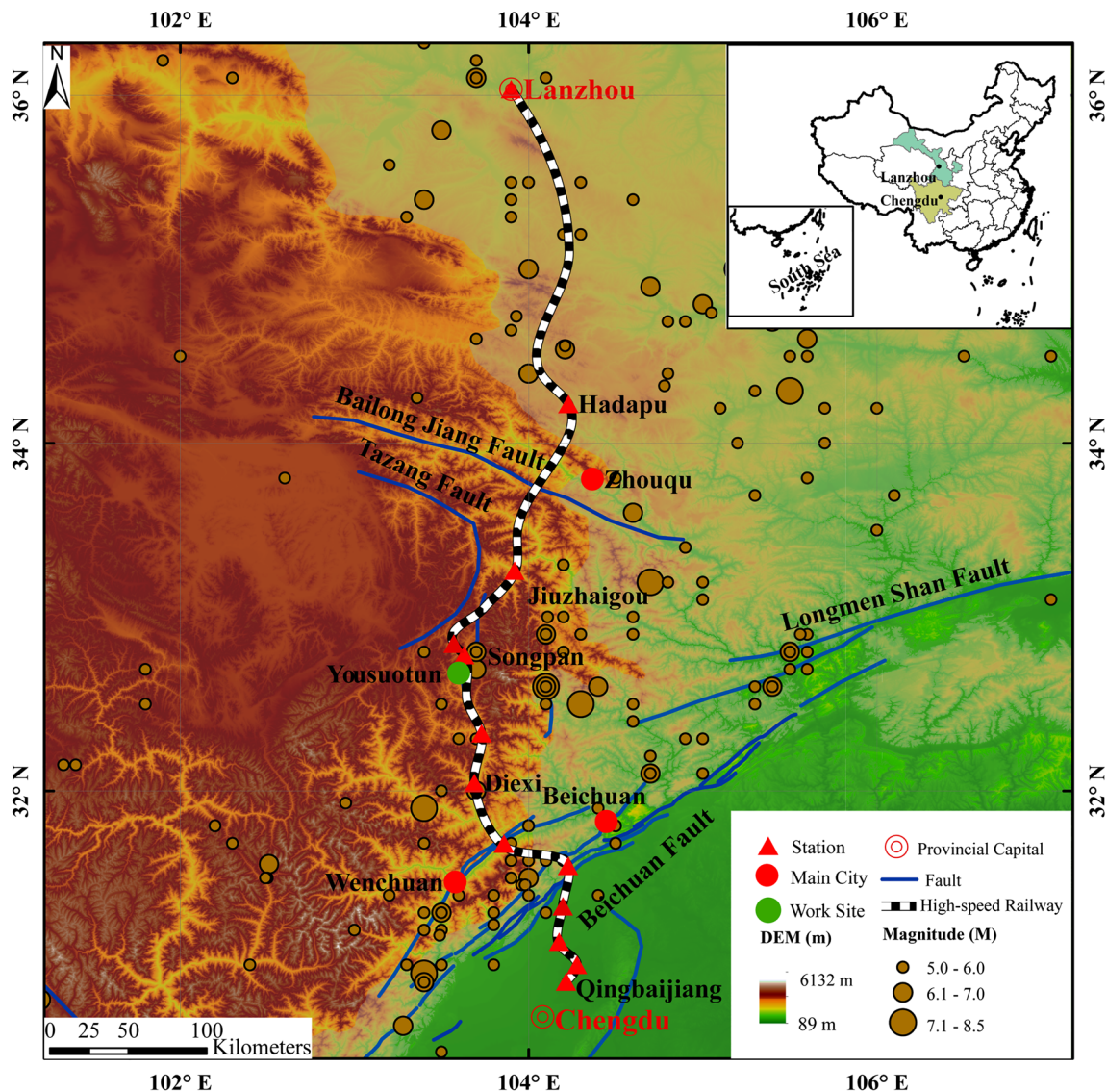


Fig. 1 The route orientation, seismic distribution, and Yousuotun test site locations of the Chenglan HSR

slope stability during earthquakes (Lirer 2012; Al-Defae and Knappett 2014). The stability of anti-slide piles within reinforced slopes is of great concern for geologists. The interaction between soil slopes and anti-slide piles under static conditions has been extensively studied (Ellis et al. 2010; Kanagasabai et al. 2011). However, according to the post-earthquake investigation of damage in Wenchuan, anti-slide piles demonstrated good anti-seismic effects, but large numbers of anti-slide piles had been tilted, overturned, or even fractured (Zhang et al. 2012). Understanding the seismic performance of anti-slide piles is the basis for improving anti-seismic design for slopes (Yu et al. 2010). To fully understand the anti-seismic mechanism of anti-slide piles, clarifying the evolution characteristics of the slope acceleration response and the dynamic strain of the anti-slide pile is necessary (Yin et al. 2015). Yu et al. (2010) studied the dynamic characteristics of pile-reinforced sand slopes under El Centro wave excitation and proposed that the overall response of pile-reinforced slopes is lower than that of nonreinforced slopes. Nian et al. (2016) derived an analytical expression that could facilitate both the calculation of the slope's yield acceleration coefficient and the improvement of the slope safety factor to the design requirement for the lateral force on the pile. Ma et al. (2019) carried out shaking table tests on two stabilizing structures for soil slopes, namely, constrained anti-slide piles and pre-stressed anchor slab-pile walls, subjected to different ground motion intensities to study the effectiveness of different stabilizing structures. Despite the above-mentioned extensive studies, the understanding of the dynamic interaction between anti-slide piles and soil slopes subjected to different ground motion intensities is still insufficient. Few studies mention dynamic model testing of anti-slide pile-reinforced bridge foundations in landslides, and only a few relevant field engineering cases can be found (Kobayashi et al. 2002).

To summarize, the geological engineers still lack a clear seismic strengthening mechanism for anti-slide piles, and in some cases, the engineering practice of the slope design in seismic areas must rely on experience to a large extent. The shortcomings of anti-slide pile-reinforced bridge foundations in landslides are summarized as follows: (1) The design of anti-slide piles remains immature as of date, especially with regard to the internal force variation in piles during seismic activity (Anderson et al. 2009). There are few related studies on the dynamic response of slopes with anti-slide piles and bridge foundations during earthquakes, and few previous engineering cases can be used as references (Kobayashi et al. 2002; Chotesuwan et al. 2012). (2) Experts in engineering geology have not gained an adequate understanding of the interactions among anti-slide piles, bridge foundations, and landslides to quantitatively describe the seismic behaviour of anti-slide piles and bridge foundations. (3) The existing design methods of anti-slide pile-reinforced bridge foundations on landslides adopted by engineers have not been able to satisfy

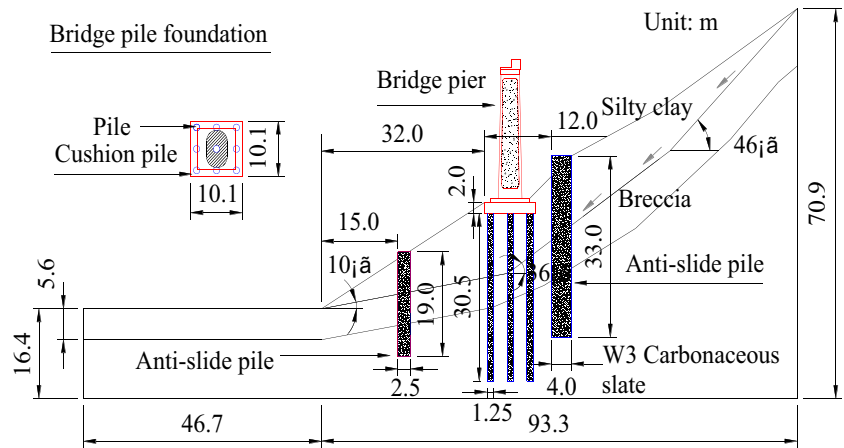
the practical needs of engineering (TB10002.5-2005; JGJ94-2008). (4) Moreover, monitoring the seismic response of co-seismic landslides is difficult because it requires the continuous accumulation of data by field stations (Medel-Vera and Ji 2016; Rong et al. 2016; Zhang et al. 2017). This requirement has led shaking table testing to become an effective method for studying the dynamic process and failure mechanisms of landslides under the effects of earthquakes (Wang and Lin 2011; Yuan et al. 2014; Shi et al. 2015; Sun et al. 2017).

The objective of this study was to clarify the seismic performances of anti-slide pile-reinforced bridge foundations in landslides by performing shaking table tests. The colluvial landslide on which the Yousuotun Bridge of the Chenglan HSR stands was selected as the prototype, and a shaking table model test of a double-row anti-slide pile-reinforced bridge foundation and landslide with a 1:40 similitude ratio was carried out. Sinusoidal waves with different frequencies and acceleration amplitudes were applied as the base excitation. Various types of sensors arranged on the slope were used to record the time-history response of the acceleration, pile strain, and dynamic earth pressure of the slope subjected to continuous multi-level seismic loads (≤ 0.7 g). Furthermore, the peak ground acceleration (PGA) amplification factor of the slope was analyzed, and the evolution characteristics of the dynamic earth pressure were studied. The results successfully revealed the response dynamic strain distribution characteristics of the anti-slide piles and the bridge foundation. In addition, this experiment clarified the anti-slide pile-reinforced bridge foundation and landslide interaction mechanism to provide a reference for bridge foundation-landslide seismic strengthening design.

Overview of the landslide

The Yousuotun Bridge along the Chenglan HSR is located in Songpan County, Sichuan Province, China. The bridge is near the DK247+788 section of the rail line, traversing the Minjiang River over three bridge spans and covering a total length of 1670 m on the eastern edge of the Qinghai-Tibet Plateau. The PGA of this region is mostly 0.2–0.3 g. The bank slope has a relief of approximately 260 m and a natural slope of 10–45°. According to the on-site investigation, the landslide at the bridge site is an ancient landslide and is in a stable state. The overall landslide is in the shape of a round-backed armchair, small at the top, and large at the bottom. The landslide body has an axial length of 100 m, a width of 40–60 m, a thickness of 3–15 m, and a volume of approximately 5×10^4 m³. This landslide is moderately sized and moderately bedded, as shown in Fig. 2. The soil in the sliding body is silty clay in a plastic state with a fine breccia layer at the bottom. The bedrock is a weakly weathered (W3) carbonaceous slate intercalated with sandstone.

Fig. 2 Cross section of Yousuotun Bridge and double-row anti-slide piles in the prototype



The bridge is located in the downslide section of the landslide. The anti-slide retaining structure consists of front-row and back-row anti-slide piles, with the bridge pile foundation in the middle. The main dimensional parameters are shown in Table 1. The bridge foundation has a diameter of 1.25 m, a pile length of 30.5 m, and a strength grade of concrete (STGC) of C30. The front-row anti-slide piles have a cross section of 2 m × 2.5 m, a pile length of 19 m, and a pile spacing of 7 m. The back-row anti-slide piles have a cross section of 3 m × 4 m, a pile length of 33 m, and a pile spacing of 7 m.

Similitude relationship

The gravity similitude law and the dimensional analysis method were used to derive the geometric size (*l*), unit weight (γ), and acceleration (*a*) as the main controlling factors (Iai 1989; Lin and Wang 2006; Liu et al. 2016); $C_r = 1$, $C_a = 1$, and $C_l = 40$. According to the similitude relationship of the physical conditions, geometric conditions, dynamic equilibrium conditions, etc., the similitude relationships, expressed as Eqs. (1)–(5), were obtained. The similitude relationship of the physical quantities was derived according to the similarity law derived by Lin and Wang (2006). Please refer to Table 3 for more details.

Shaking table model test design

Test apparatus

The test was carried out on an electro-hydraulic servo-driven seismic simulation shaking table with a platform size of 4 m × 2 m and a horizontal excitation at Southwest Jiaotong University (SWJTU). The maximum load on the table is 25 tons, the maximum horizontal displacement is ± 100 mm, and the maximum acceleration is 1.2 g at full load. The acceleration repeatability of the actuator is ± 3%. The size of the rigid model box is 3.7 m × 1.5 m × 2.1 m (length × width × height). The back wall of the model box is lined with an 8-cm-thick foam carpet to reduce the reflection of seismic waves at the boundary (Fang et al. 2003). The primary performance parameters of the shaking table are listed in Table 2.

$$\frac{C_c}{C_1 C_\gamma} = 1 \tag{1}$$

$$\frac{C_a}{C_1 C_w^2} = 1 \tag{2}$$

$$\frac{C_\sigma}{C_1 C_\gamma} = 1 \tag{3}$$

$$\frac{C_g}{C_1 C_w^2} = 1 \tag{4}$$

$$C_w C_T = 1 \tag{5}$$

where $C_s = C_l$, $C_\varepsilon = 1$, $C_\varphi = 1$, and $C_\mu = 1$; *l* is the geometric size, *c* is the cohesion, φ is the internal friction angle, γ is

Table 1 The dimensional parameters of the Yousuotun Bridge and anti-slide piles in prototype

Structure	Length (m)	Sectional dimension (m)	Axis spacing (m)	STGC	Distance from toe (m)
Front-row anti-slide pile	19	2.0 × 2.5	7	C40	15 m
Back-row anti-slide pile	33	3.0 × 4.0	7	C40	44 m
Bridge foundation	30.5	Diameter 1.25	3.9	C30	/
Bridge cushion cap	2	10.1 × 10.1	/	C30	32 m

Table 2 Performance parameters of the shaking table

Shaking table size	Max. load (t)	Max. acceleration (g)	Range of frequency (Hz)	Max. displacement (mm)	Wave form	Driving way
4 m × 2 m	25	Horizontal 1.2	0.4–15.0	Horizontal ± 100	Regular/seismic wave	Electro-hydraulic servo

the unit weight, μ is the dynamic Poisson’s ratio, g is the gravitational acceleration, T is the time, ω is the frequency, s is the linear displacement, ε is the strain, σ is the stress, and a is the PGA.

Model construction

The slope model consisted of a landslide body (silty clay), a landslip layer (weak interlayer), a lower breccia layer, and bedrock. The modelling materials were all taken from the actual project site. The silty clay was crushed and passed through a 5-mm sieve. The water content was adjusted to 25.6%, and after 24 h of curing, the landslide body was filled with the modelling materials. The gradation curve of the filling soil is shown in Fig. 3. The dry density of the landslide body was controlled at 1.90 g/cm³. The large-scale direct shear test was used to determine, under the undrained condition, the internal friction angle of the silty clay, which was 14.0° and the cohesive force, which was 20.4 kPa. The internal friction angle of the breccia soil was 35.1°. The physical and mechanical parameters of the slope material are shown in Table 4. The 1.0-cm-thick landslip zone created a smooth contact surface, which was made of a 1:2 mixture of bentonite and fine sand. The breccia layer was simulated by a mixture of coarse gravel and crushed stones. The bedrock was made of

red clay, cement, quartz sand, and water with a ratio of 1:0.55:1:0.25 to ensure an elastic modulus of 16.4 GPa. To effectively reduce the friction effect on the inner wall of the model box, the plexiglass on both sides of the inner walls was cleaned, and Vaseline was evenly coated on the plexiglass. A smooth layer of transparent cellophane was pasted on the sidewalls as a friction-reducing membrane. Then, another thin Vaseline layer was applied to the surface of the cellophane, and the slope model was filled in layers. These procedures can effectively reduce the friction effect between the slider and the box wall during the vibration process (Haeri et al. 2012; Li et al. 2019).

The back-row anti-slide piles were located in the downslide section of the landslide, while the front-row anti-slide piles were located in the landslide-resistant section. The reinforcement ratio and the stirrup ratio of the actual bridge pile foundation and the anti-slide piles were adopted to create a model composed of micro-concrete. With reasonable control of the aggregate dosage and water-cement ratio, the mechanical properties of the micro-concrete showed satisfactory similitude with the ordinary concrete in the prototype (Brara and Klepaczko 2007; Li et al. 2014). The dimensional parameters of the model structures are displayed in Table 5. A 40-cm-high gravity pier was placed on the upper part of the pile cap. Given the dynamic influence of the bridge superstructure on the

Table 3 Similarity relationship and scaling factors for the shaking table tests in this study

Parameter type	Physical quantity	Dimension	Similarity ratio (prototype/model)	Remarks	
Physical dimension	Length (l)	C_l	40	Control variable	
	Displacement (s)	$C_s = C_l$	40		
Material characteristics	Mass density (ρ_s)	C_ρ	1	Control variable	
	Unit weight (γ)	C_γ	1		
	Cohesion (c)	$C_c = C_\rho C_l$	40		
	Internal friction angle (φ)	$C_\varphi = 1$	1		
	Strain (ε)	C_ε	1		
	Stress (σ)	$C_\sigma = C_\rho C_l$	40		
Dynamic characteristics	Poisson’s ratio (μ)	C_μ	1	Control variable	
	Gravity acceleration (g)	C_g	1		
	Input acceleration (a)	C_a	40		Input control
	Shaking time (t)	$C_t = (C_a/C_l)^{-0.5}$	40		Input control
	Frequency (f)	$C_f = (C_a/C_l)^{0.5}$	1		

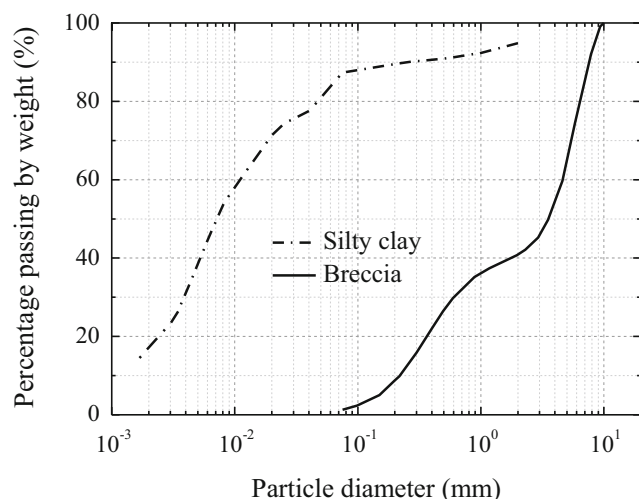


Fig. 3 Particle-size distributions of breccia soil and silty clay

bridge foundation, a prefabricated steel box was fixed on top of the bridge pier to simulate the movable beams. A track was welded along the central axis of the steel box to allow the double weights to slide freely. Two weights were hung at a certain distance along the track to simulate the simply supported box girders on either side of the pier top (Tang et al. 2010). The weights were determined as per the experimental similarity relation in Fig. 4(b) and (c). The anti-slide piles and bridge pile foundation were prefabricated and cured. The model after filling is shown in Fig. 4(f). The slope model was filled layer upon layer and levelled and tamped from the bottom up.

Instrumentation

The arrangements of the sensors in the model are shown in Fig. 5. The accelerometers were placed behind the back-row anti-slide pile P3, as well as between the front-row anti-slide pile P1 and the bridge foundation P2. The model was equipped with 11 sets of accelerometers (at points A1–A11) using German-made ICP/IEPE piezoelectric horizontal accelerometers with a working frequency of 0.1–100 Hz and a measuring range of 2.0 g. Point A10 on the table base was used to record the actual input acceleration of the shaking table. A total of 17 dynamic earth pressure sensors (at points E1–E17) were arranged at the front and rear of the front- and back-row anti-slide piles, as well as at the front side of the bridge foundation. Earth pressure mini-sensors with a diameter of 10 mm, a thickness of 5 mm, and a range of

100 kPa were used. Strain gauges configured with a quarter bridge were arranged symmetrically on the front and rear sides of the anti-slide piles and the pier foundation pile, and strain was measured at a total of 21 points (S01–S21). Five YHD-100 pull-rod displacement meters (at points D1–D4) were used to monitor the horizontal displacement of the sliding surface with an accuracy of 0.001 mm. The sensors were all calibrated prior to installation.

Seismic wave input

To simulate the damaging effects of seismic waves with different frequencies and PGAs on the landslide model, sinusoidal waves with frequencies of 3 Hz and 10 Hz, which would not cause resonance in the model, were selected as the seismic excitation. A similar input motion of sine waves was employed by Lin and Wang (2006), Torisu et al. (2010), Pal et al. (2012), and Liu et al. (2016). The input acceleration amplitude was increased from 0.08 to 0.7 g. A micro-vibration test of 0.08-g white noise excitation was used to determine the dynamic properties of the slope materials. The loading scheme of the seismic wave is shown in Fig. 6. The input seismic waveform is shown in Fig. 7. The duration of the earthquake was compressed to 1/6.32 of that experienced by the prototype. The measured data were converted to the actual results of the prototype according to the similarity in Table 3.

Seismic behaviour of a bridge-pile-foundation slope

This section first introduces the apparent characteristics of the slope model after the earthquake, then analyzes the responses of acceleration, dynamic earth pressure, and dynamic strain, and finally summarizes the anti-seismic mechanism of the anti-slide pile-reinforced bridge foundation.

Post-earthquake indicative characteristics

After loading the PGA of 0.7 g, the bridge foundation and landslide exhibit no obvious signs of damage, and the bridge foundation is stable, as shown in Fig. 8a. The peak displacement of the slope increases with increasing PGA. Affected by the landslide thrust, the dynamic displacements of the pile tops

Table 4 The physical and mechanical properties of the model slope material

Stratum	Unit weight (kN/m ³)	Cohesion c (kPa)	Internal friction angle φ (°)	Water content (%)	Poisson's ratio ν	Elasticity modulus E (MPa)
Silty clay	19.0	20.4	14.0	25.6	0.40	10.0
Breccia	21.0	0	35.1	16.6	0.30	100.0
Bedrock	23.0	1.8×10^3	40.0	4.0	0.24	5.1×10^4

Table 5 Structural dimensions of the bridge foundation and anti-slide piles in the model

Structure	Quantity	Length (cm)	Sectional dimension (cm)	Pile spacing (cm)	STGC
Front-row anti-slide pile P1	7	47.5	5.0 × 6.25	17.5	C40
Back-row anti-slide pile P3	9	82.5	7.5 × 10	17.5	C40
Bridge foundation P2	3 × 3	76.25	Diameter 3.125	9.75	C30
Bridge cushion cap	1	5.0	25.25 × 25.25	/	C30

of the back-row anti-slide piles are greater than those of the front-row anti-slide piles. The anti-slide piles significantly reduce the displacement of the bridge foundation, as shown in Fig. 8c. When the input PGA is less than or equal to 0.4 g, the maximum dynamic displacement of the bridge foundation is 0.4 mm. The displacement of the landslide body accumulates under the amplitude increase during repeated earthquakes. The markings on the sidewall of the model box show that the landslide has slid along the landslip surface, as shown in Fig. 8b.

Figure 9 shows the spectrum analysis curve of the slope material in the 0.08-g white noise test. When the Gaussian white noise propagates upward, a filtering process occurs in the spectral response of the soil, and the amplitude of the spectrum near the natural frequency is amplified. The response amplitude of the spontaneous vibration frequency of

the silty clay is larger than that of the fine breccia. The response interval for the first natural frequency of the model is 11–29 Hz, while it is 32–39 Hz for the second natural frequency. The first and second natural frequencies of silty clay are 20.4 Hz and 34.1 Hz, respectively.

Acceleration response

The response acceleration is a main parameter that characterizes the instability of the slope caused by the inertial force. The acceleration distribution characteristics of the key points of the slope, including points A2, A5, A6, and A9 on the slope surface and points A1, A4, and A8 on the soil-rock interface of the slope, were obtained to analyze the effect of acceleration amplification on the slope.

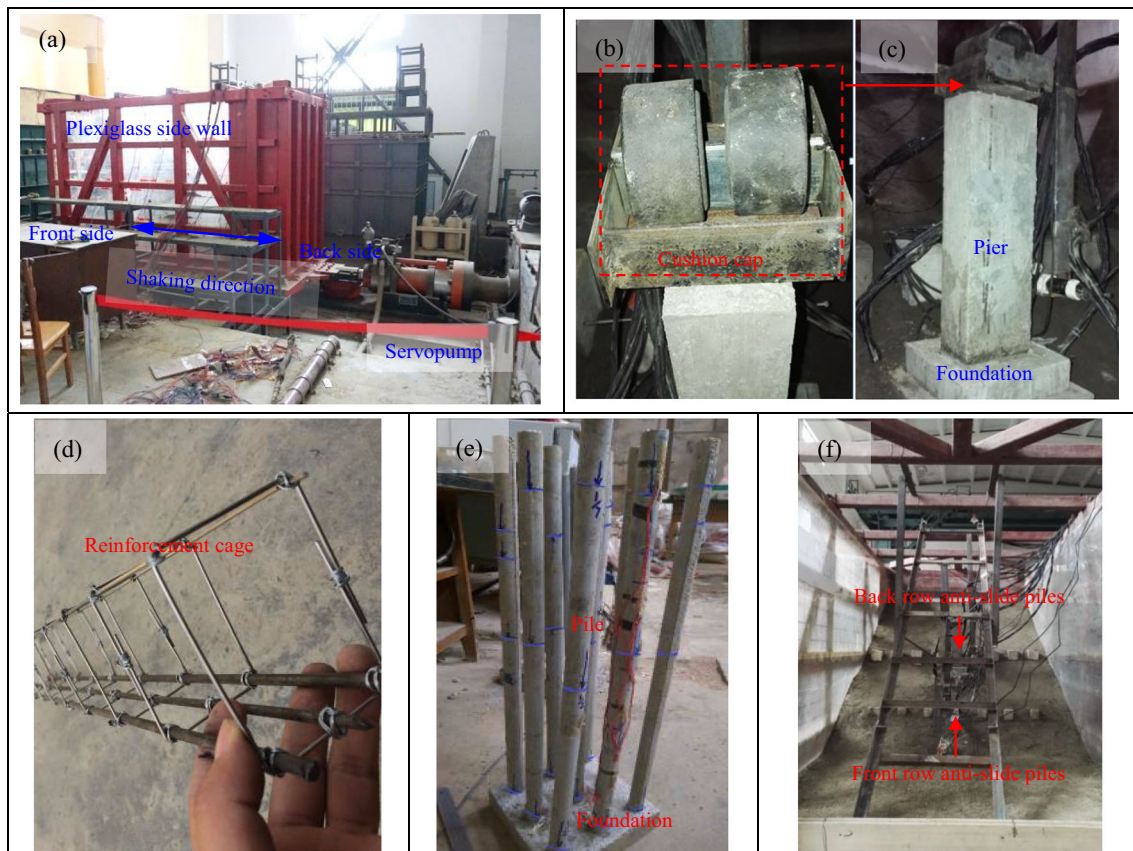


Fig. 4 Photographs of the slope model for the shaking table test. (a) Shaking table; (b) movable beams; (c) piers and cushion cap; (d) reinforcement cage of anti-slide pile; (e) bridge pile foundation; (f) completed model and displacement sensor bracket

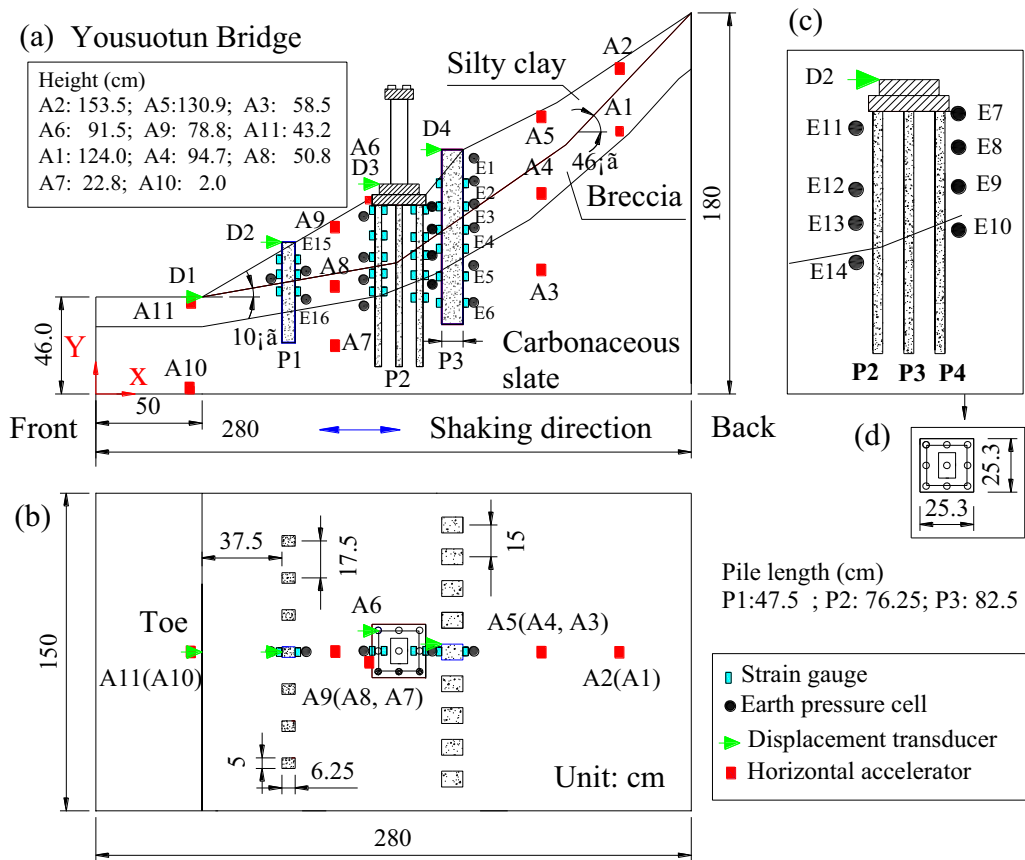


Fig. 5 Schematic of the monitoring arrangement in the model and model dimensions (unit: cm). (a) Cross section of the model; (b) horizontal layout of the model; (c) earth pressure cell of the bridge foundation; (d) horizontal layout of the bridge cushion cap

Variations of acceleration with the input PGA

Taking point A2 in the downside section of the landslide as an example, the acceleration value a_{max} is the weighted mean of the acceleration amplitude of the landslide. The acceleration-time curve when PGA is 0.6 g is presented in Fig. 10. Figure 11 shows the relationship curve of the input

acceleration amplitude and the response PGA obtained from point A10. With the increase in the ground motion intensity input by the actuator, the PGA of point A10 increases, indicating that the performance of the shaking table meets the loading requirements for the ground motion intensity. As the input PGA increases, the response acceleration of each measuring point increases.

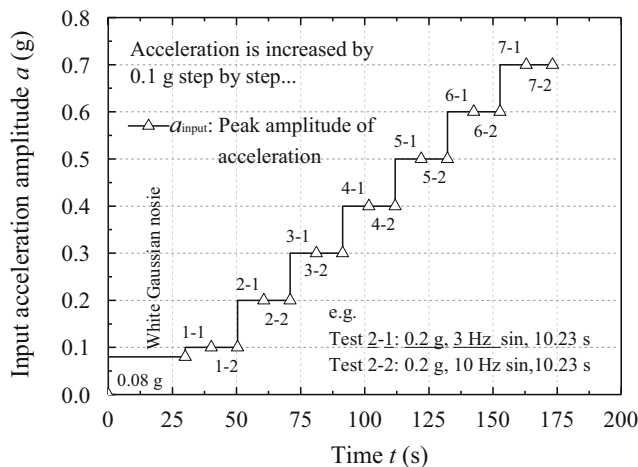


Fig. 6 Input acceleration amplitude converted by the prototype wave to the vibration shaker with time

Acceleration amplification effect

The ratio of the horizontal monitoring acceleration amplitude in the slope to the actual input acceleration amplitude of the table (measuring point A10) is defined as the PGA amplification factor (Srilatha et al. 2013). Figure 12 shows a distribution contour plot of the PGA amplification factors of the slope. With increasing input acceleration amplitude, both the dynamic response of the slope and the PGA amplification factor increase. The PGA amplification factor shows a layered distribution along the downhill direction of the slope. A PGA of 0.5 g is defined as the boundary intensity between moderate- and high-intensity earthquakes (GB18306- 2001 2001). Figure 12a–c show that the fine breccia layer at the slope foot can effectively dissipate the energy of the vibration wave during the vibration, and the PGA amplification factor is small.

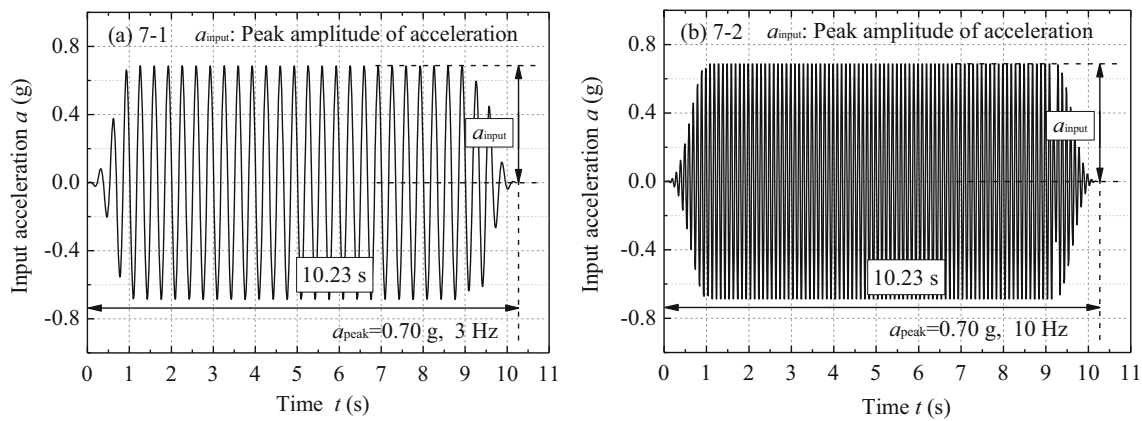


Fig. 7 Compressed acceleration-time curves of input sinusoidal waves with a PGA of 0.7 g. **a** 3 Hz. **b** 10 Hz

When $PGA \leq 0.4$ g, the PGA amplification factor of the shallow layer (2.4-m deep) on the back side of the bridge foundation is larger than that of the deep layer. For the back-row anti-slide pile P3, the PGA amplification factor in front of pile is smaller than that behind the pile. When $PGA \geq 0.5$ g, the seismic response of the landslide body on the back side of pile P3 is enhanced, as shown in Fig. 12b and c. The PGA amplification factor on the front side of the pier also increases with the increase in the ground motion intensity. In Fig. 12, the yellow-green region, representing a strong amplification of the PGA, spreads to the breccia layer (12 m), which is consistent with the sliding phenomenon observed in the landslide body shown in Fig. 8b. Viscous damping occurs due to the dissipation of frictional energy when the shear wave propagates through the rock and soil mass. If the distance between the bridge foundation and pile P3 is too small, the energy dissipated by the back-row anti-slide piles during seismic wave propagation is limited; thus, a reasonable pile spacing should be set.

Figure 13a and b show the PGA amplification factors of the landslide. The soil demonstrates a series of amplification effects in the epicentre and exhibits a nonlinear state (Hashash et al. 2015; Liu et al. 2016). The PGA amplification factor has

a significant nonlinear amplification effect along the elevational direction of the slope. The PGA amplification factor of point A2, which is at the crest of the slope, ranges from 1.16 to 1.32 when $PGA \leq 0.7$ g, while the PGA amplification factor at the foot (A11) is 0.96–1.06. The higher the position on the slope, the stronger the PGA response and the more obvious the PGA amplification effect are (Xu et al. 2010). Due to the high and steep-free surface of the landslide backwall, the PGA of point A2 reaches its maximum value, showing an obvious PGA “elevation effect”.

For the soil mass at the same elevation, the seismic wave produces a magnification effect on a single-free-face slope, with a larger effect on the surface layers (A5) than in the deeper layers (A1). The PGA amplification effect is found to be greater along the slope surface, which is expressed as the “surface effect”, that is, the closer the position is to the slope surface, the larger the PGA amplification factor. Since the shallow soil in the slope surface is less constrained, it is more likely to vibrate strongly under a seismic wave from the bed-rock. As the slope elevation increases, the increasing trend of the PGA amplification factor near the bridge foundation slows (Fig. 13b), indicating that the seismic response of the anti-slide piles and the soil surrounding the bridge foundation is

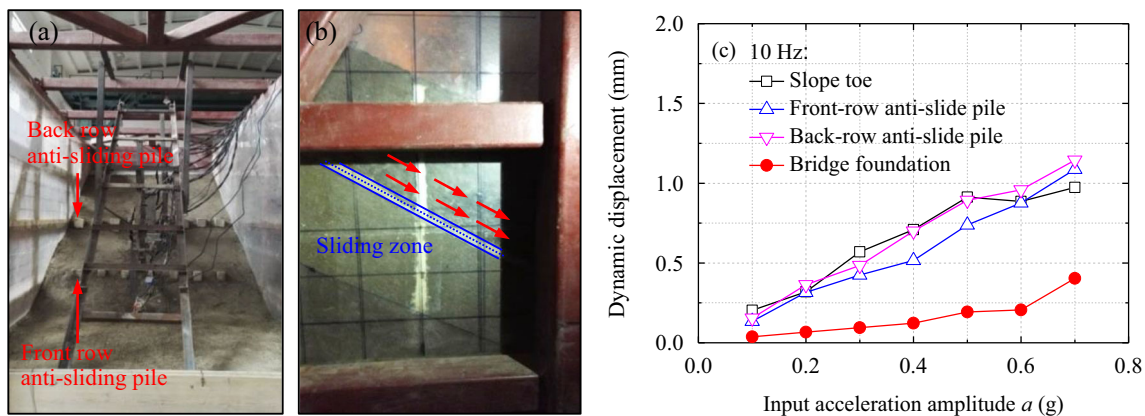


Fig. 8 Apparent characteristics and the dynamic displacement of the slope model after a PGA of 0.7 g is applied. **a** The model does not undergo significant damage. **b** The landslide body slides along the landslip surface. **c** The variation in peak displacement with input PGA

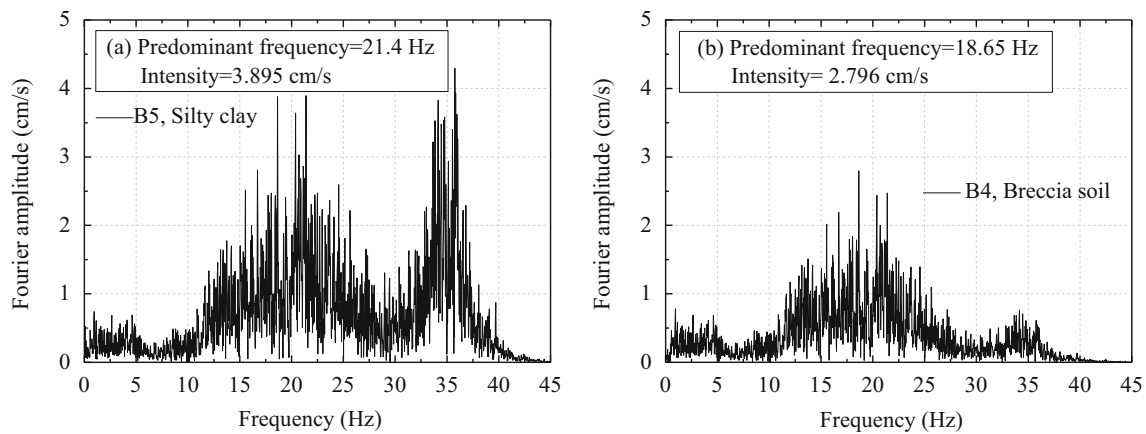


Fig. 9 a, b Spectrum analysis of the natural vibrations in the landslide mass

suppressed. The anti-slide piles and the bridge foundation can reduce the acceleration amplification effect of the slope surface to a certain extent and weaken the seismic response of the slope. This process occurs because the reinforcement effect of the anti-slide piles and the soil arching effect between the piles can limit the dynamic response of the reinforcement area and reduce the response acceleration. In addition, the anti-slide piles produce a reflection superposition effect of the seismic waves in the landslide deposit, with a larger response acceleration in front of piles than that behind piles.

Figure 13 c illustrates the PGA amplification factor curve of the rock and soil interface inside the slope. The seismic response inside the landslide is affected by the properties of the slope material, which is manifested as a “geological structure effect”. The PGA amplification factor of point A1 on the landslide bed ranges from 1.10 to 1.21, which is smaller than that of the landslide body (A5). The maximum PGA amplification factor of the bedrock is only 1.05, demonstrating a smaller response. At the same elevation, the breccia layer (A8) has a larger amplification effect than that of the bedrock (A3). For the geological structure with soft top and hard bottom layers, the amplification due to the “geological structure effect” is obvious.

Figure 13 d shows the effect of seismic frequency f on response acceleration. The PGA amplification effect of the slope is stronger at 10 Hz than at 3 Hz. The PGA amplification factors corresponding to low excitation frequencies were considerably lower than those for high excitation frequencies. This phenomenon is consistent with the results proposed by Brennan and Madabhushi (2009), Roten et al. (2013), and Lin et al. (2018). Seismic waves generate viscous damping when propagating through the rock and soil, and the damping is proportional to the velocity of the material. For a consistent input PGA, the PGA amplification factor is related to the seismic frequency. The higher the frequency is, the smaller the velocity of the granular particles (Hobiger et al. 2012), which in turn leads to less viscous damping of the soil and a larger PGA amplification factor (Brennan et al. 2005; Hashash and Park 2002).

Figure 14 shows the variations in the PGA amplification factor with the input acceleration amplitude at 10 Hz. When $\text{PGA} \leq 0.3$ g, as the input acceleration amplitude increases, the acceleration responses measured at points A3, A4, A5, and A6 along the slope crest decrease, and the PGA amplification factor decreases. A similar phenomenon was found in other 1-g large-scale shaking table tests of slopes (Xu et al. 2008),

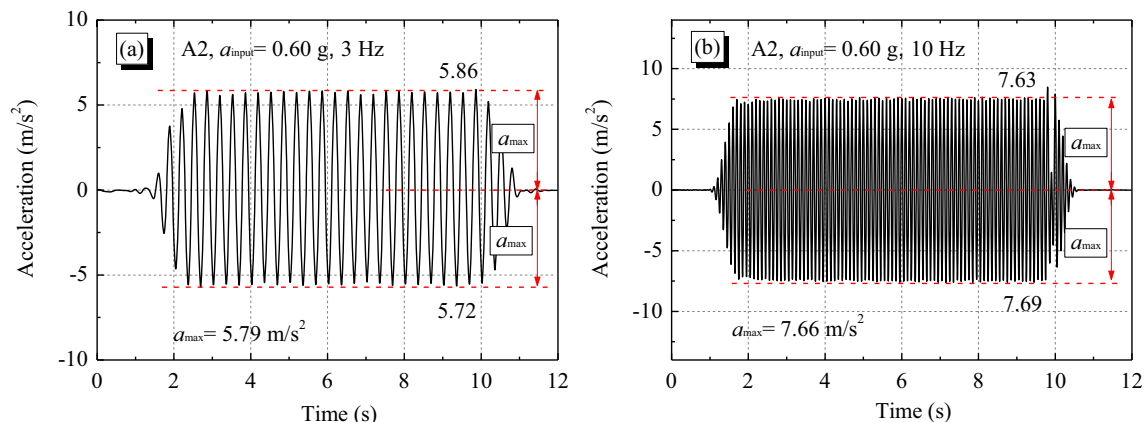


Fig. 10 Time-history curves of the acceleration at A2 on the surface of the landslide body under a PGA of 0.6 g. a 3 Hz. b 10 Hz

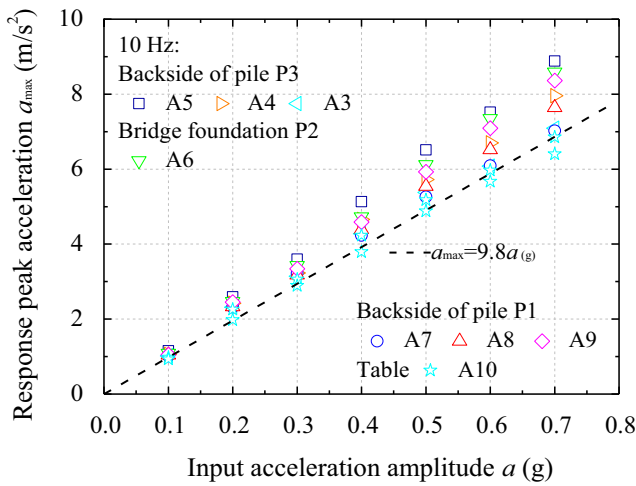


Fig. 11 Relationship between the input PGA of the shaking table and the response acceleration as monitored from the slope

that is, the deposit body shows obvious nonlinear characteristics when subjected to dynamic loading (Sun et al. 2015). On the one hand, with increasing ground motion intensity, the shear strain of the soil increases, the stiffness modulus decreases, and the damping ratio increases, which reduces the PGA amplification factor. On the other hand, loose deposit bodies show a tendency towards vibratory compaction under continuous low-intensity earthquakes, which also reduces the

PGA amplification effect. When $PGA \geq 0.4$ g, the slope is subjected to greater seismic inertial force, which causes the landslide interior to gradually loosen. This effect further causes the sliding deformation of the landslide body to develop, the dynamic response of the slope to increase, and the PGA amplification factor to rise rapidly. The response acceleration of the bedrock (A3) with a PGA amplification factor of 1.03 is not significantly affected by the input PGA.

Dynamic earth pressure response

Variation in dynamic earth pressure with input PGA

The dynamic earth pressure on the back side of the reinforced structure affects not only the stability of the structure but also the stability of the soil mass around the structure (Ma et al. 2019). Figure 15 shows the variation in the dynamic earth pressure response with time for the back-row anti-slide pile P3 at point E1. When only the increase in structural earth pressure caused by an earthquake is considered, the dynamic earth pressure peak σ_{dmax} is the weighted average of the positive and negative peak values of the earth pressure in the landslide direction. Figure 16 shows the vector distribution characteristics of the dynamic earth pressure peak of the anti-slide piles (back-row P3, front-row P1) and the bridge

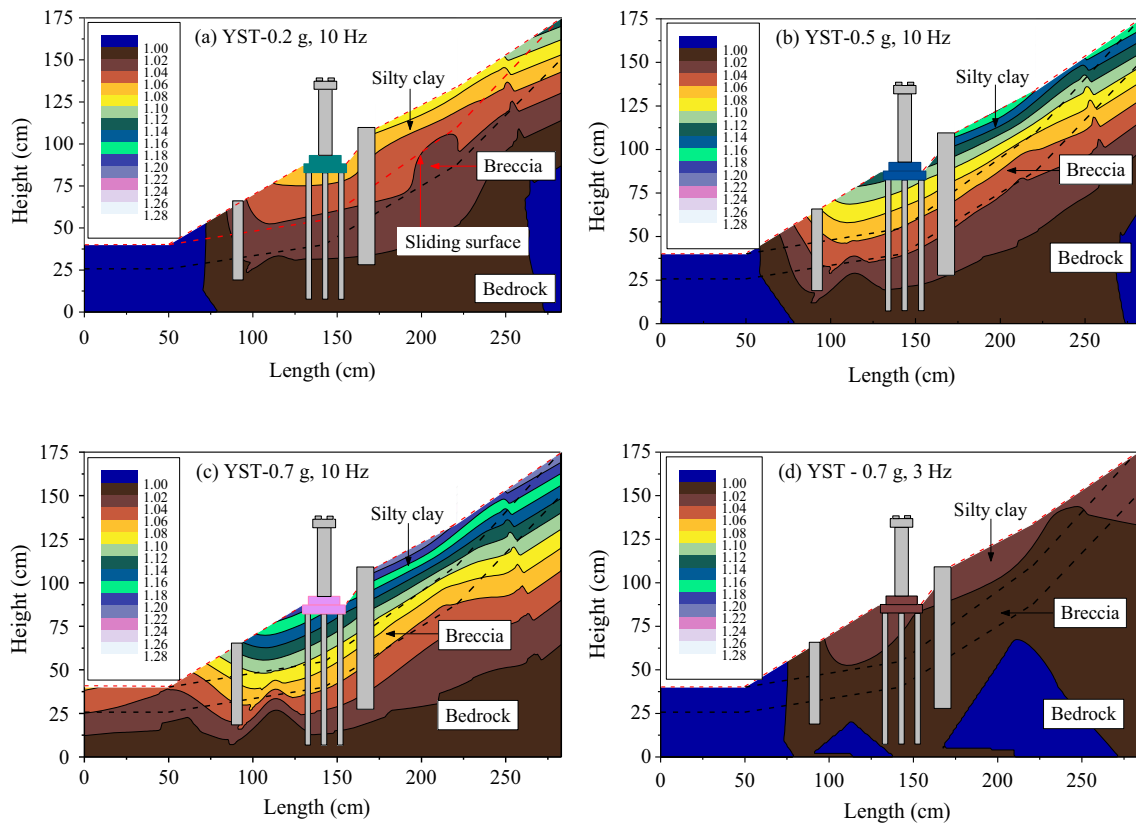


Fig. 12 PGA amplification factor distribution contour plots of the slope with input acceleration amplitude. **a** 0.2 g and 10 Hz. **b** 0.5 g and 10 Hz. **c** 0.7 g and 10 Hz. **d** 0.7 g and 3 Hz

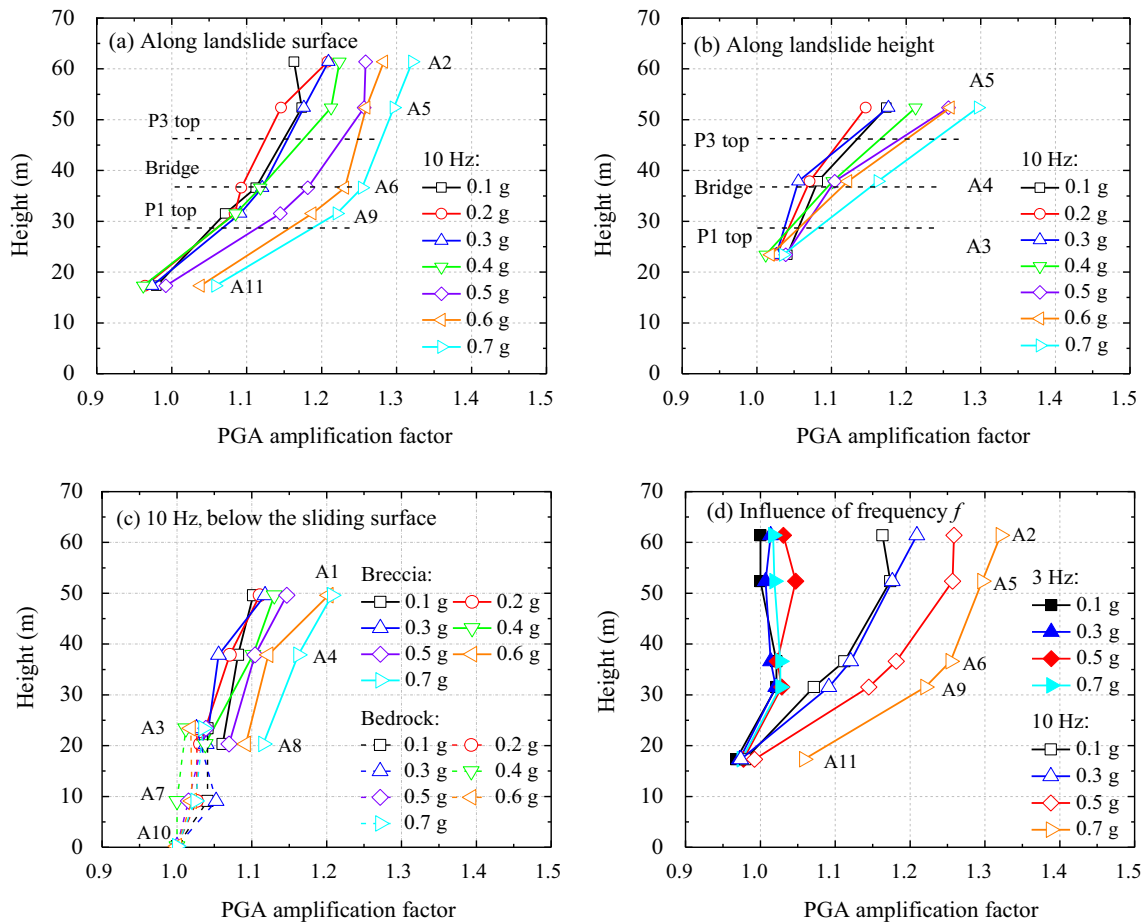


Fig. 13 PGA amplification factor of the slope at the key measurement points distributed along the elevation under the $f = 10$ Hz condition. **a** Acceleration distribution of the landslide. **b** Vertical distribution of

acceleration. **c** Acceleration distribution of breccia and bedrock. **d** Influence of frequency on acceleration

foundation P2 with the input PGA. As shown in Fig. 16, the distribution of the dynamic earth pressure of pile P1 shows a shape with “a large bottom and a small top”. Moreover, the

distribution of dynamic earth pressure on the front side of the bridge foundation P2 is “small in the middle and big at the ends”.

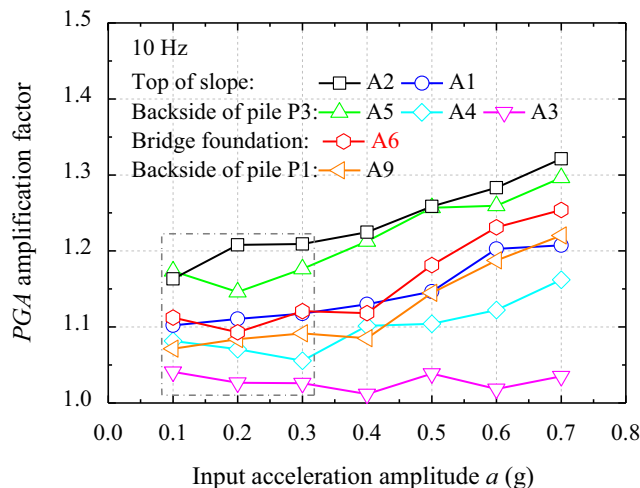


Fig. 14 Variations in the PGA amplification factor at key points inside the slope with an input acceleration amplitude at $f = 10$ Hz

Figure 17a shows the variation in the response peak of the dynamic earth pressure on the back side of anti-slide pile P3 with the input acceleration amplitude. The response peak of the dynamic earth pressure of the load-bearing section (depth < 6.8 m) increases as the input PGA increases. When the input PGA is less than or equal to 0.3 g, the response peak of the dynamic earth pressure is maximum at point E3. When $PGA \geq 0.4$ g, the dynamic earth pressure of the load-bearing section increases significantly. This result shows that with the increase in the seismic response of the slope, the supporting performance of anti-slide piles is gradually strengthened. The dynamic earth pressure of the embedded section (depth > 6.8 m) remains unchanged, with a maximum of 19.8 kPa. As the input PGA increases, the position with the maximum peak value of the dynamic earth pressure shifts up, resulting in a larger value at point E1 than at point E3.

Figure 17b shows the variations in the maximum value of the dynamic earth pressure of pile P3, bridge foundation P2,

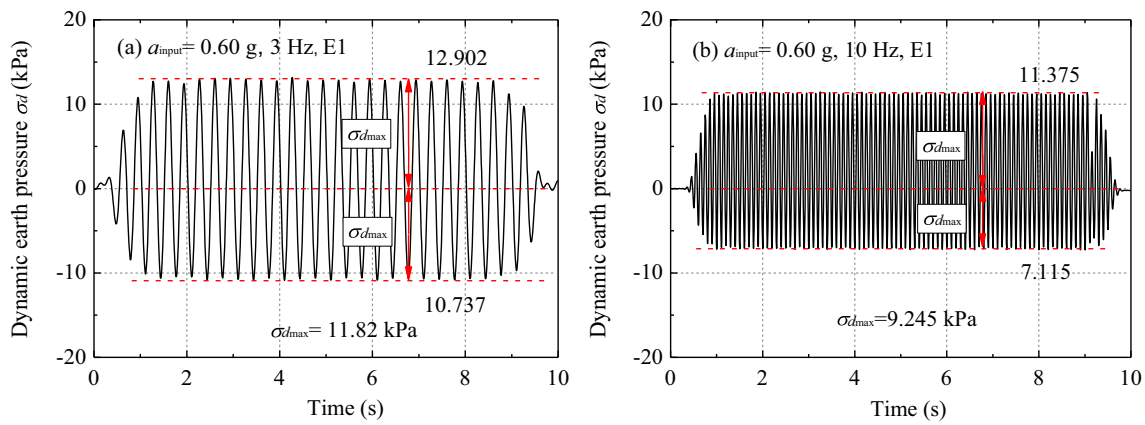


Fig. 15 Dynamic earth pressure-time curves of measurement point E1 when the input PGA is 0.6 g. a 3 Hz. b 10 Hz

and pile P1 with the input PGA. The maximum dynamic earth pressure appears at point E1 of pile P3. The maximum value of the dynamic earth pressure of bridge foundation P2 occurs at point E14 (a front-row pile) and point E7 at the back-row pile. The maximum dynamic earth pressure between piles P2 and P3 is 11.3 kPa, that is, the bridge foundation P2 is weakly affected by the thrust of the back side of the landslide. The maximum dynamic earth pressure between pile P2 and pile P1 is 55.6 kPa.

Dynamic earth pressure distribution along pile depth

Figure 18a shows that the peak value of the dynamic earth pressure behind the back-row anti-slide pile P3 is distributed along the pile depth. The 3-Hz sinusoidal wave produces greater peak earth pressure behind pile P3 than that of the 10-Hz wave. When the same PGA is applied, the low-frequency wave (3 Hz) can cause the soil to undergo more displacement deformation, which produces a stronger landslide thrust. As shown in Fig. 18a, the response of dynamic earth pressure can be divided into two parts by a sliding surface (depth of 12.6 m). When $PGA \leq 0.3$ g, the maximum

dynamic earth pressure is in the middle of the landslide, and the landslide thrust distribution is in a shape of a spoon along the pile depth, that is, low at both ends and high in the middle. When $PGA \geq 0.4$ g, the dynamic earth pressure of the upper part of the pile body increases rapidly, and the dynamic earth pressure is distributed along the pile depth in the shape of a bow. The landslide thrust is mainly borne by the upper part of pile P3. The action points of the resultant force of the dynamic earth pressure move to the top of the piles as the input PGA increases. The reason for the upward shift of the resultant action point of the landslide thrust is that the seismic wave has an amplification effect on the slope surface, causing a strong dynamic response in the nearby soil and resulting in an increase in the earth pressure on the pile. As the input PGA increases, the soil arching effect between the piles leads to a redistribution of the pile-soil stress, and the landslide thrust is also transferred to the upper part of the piles. The breccia layer behind the piles is relatively stable, and point E4 is subjected to a very low dynamic earth pressure. To restrain the deformation of the back-row anti-slide pile P3, the earth pressure of the bedrock anchoring section (E5–E6) must be less than 29 kPa. Under the action of the earthquake, the landslide

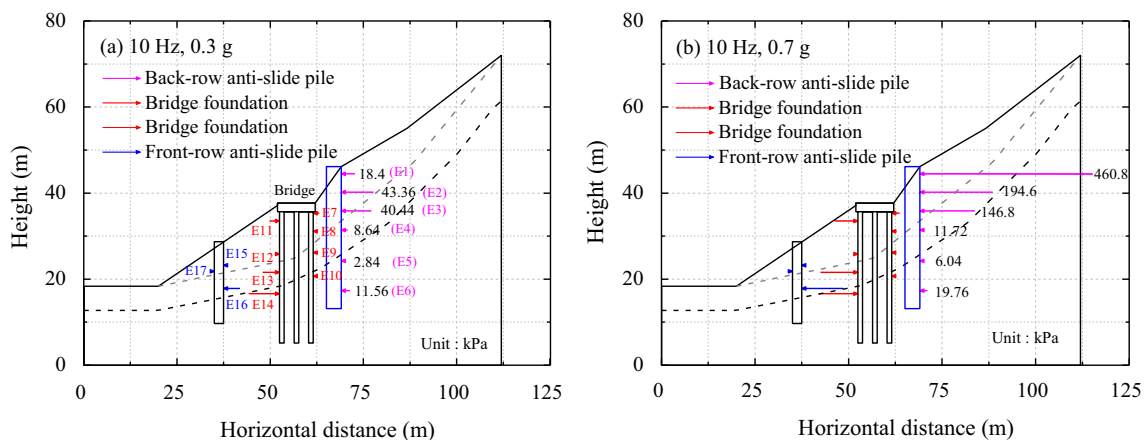


Fig. 16 Vector distributions of the dynamic earth pressure peak of the anti-slide piles and the bridge foundation with the following ground motion intensities. a 10 Hz and 0.3 g. b 10 Hz and 0.7 g

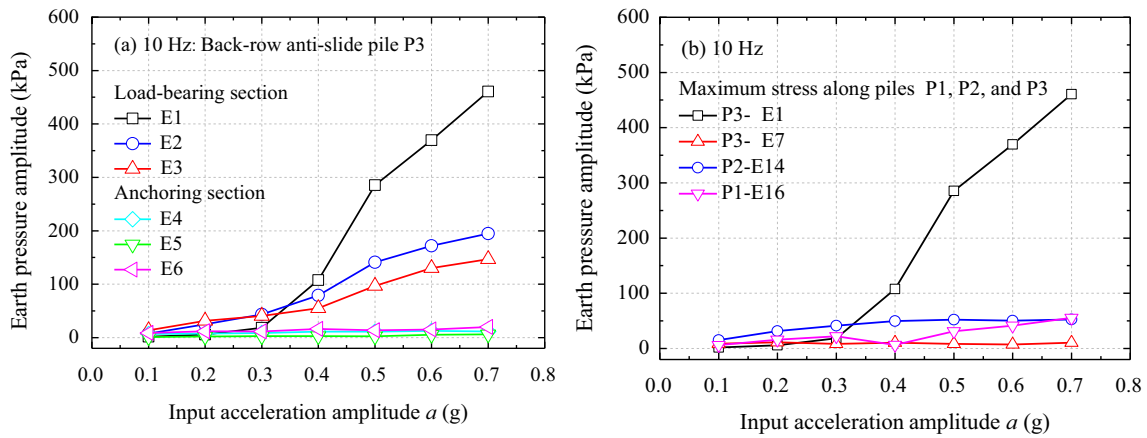


Fig. 17 Variations in the peak dynamic earth pressure of the slope with input PGA. **a** Measuring points E1-E6 behind pile P3. **b** The maximum earth pressures of piles P1 and P3

thrust is mainly borne by the middle and upper parts of pile P3 when the slope approaches the slide. The traditional design aims to strengthen the middle and lower parts of the pile body, which are the most prone to damage in seismic design.

Figure 18b shows the peak dynamic earth pressure distributed along the pile between the bridge foundation P2 and back-row anti-slide pile P3. As the input PGA increases, the

dynamic earth pressure between piles P2 and P3 increases slowly with a low earth pressure. The maximum value at point E7 is only 10.7 kPa. The dynamic earth pressure is distributed along the pile in a triangular shape, characterized by a large top and a small bottom. The pressure difference between the front and back sides of pile P3 is significant, indicating that the anti-slide effect and arching effect of pile P3 limit the transfer

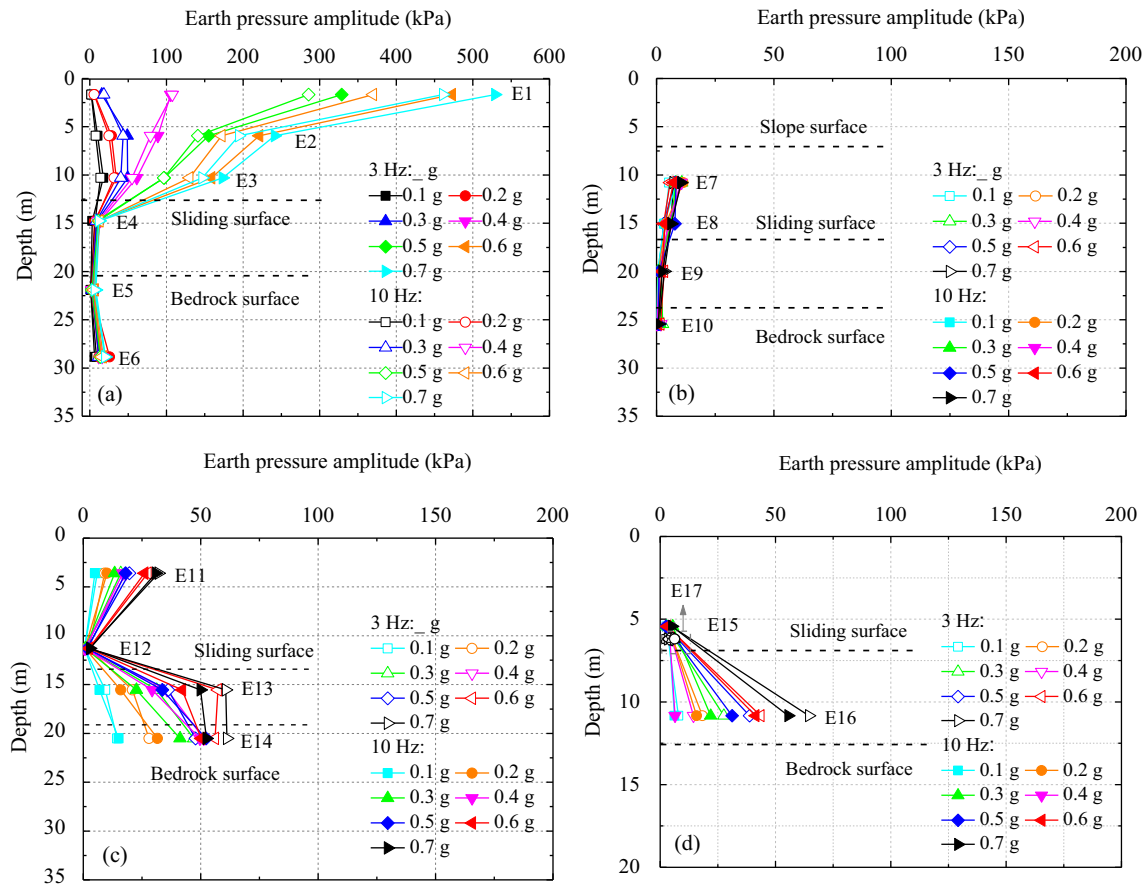


Fig. 18 The distributions of the peak dynamic earth pressure of the pile with pile depth when subjected to different input PGA. **a** Behind back-row anti-slide pile P3. **b** Between pile P3 and the bridge foundation P2. **c** The front side of the bridge foundation P2. **d** Front-row anti-slide pile P1

of the dynamic earth pressure from the landslide body to the bridge foundation. Figure 18c shows the distribution of the peak dynamic earth pressure at the front side of the bridge foundation P2 along the pile depth. The peak value of the dynamic earth pressure in the landslide exhibits a triangular distribution characterized by a large top and a small bottom. The dynamic response of E11 at the slope surface is enhanced, and the dynamic earth pressure is increased, while the dynamic earth pressure of the sliding surface (E12) is very low. The anchoring section of the bridge foundation (E14) has the highest dynamic earth pressure and can effectively restrain the deformation of the bridge foundation. The dynamic earth pressure of the breccia layer (E13) increases rapidly. As the input PGA increases, the dynamic earth pressure of E13 gradually approaches that of E14. The dynamic earth pressure distribution of the anchoring section changes from triangular (with a small top and a large bottom) to trapezoidal.

Figure 18d shows the dynamic earth pressure of pile P1 with pile depth. The dynamic earth pressure in the landslide is very small. The dynamic earth pressure of the breccia layer increases with increasing input PGA, forming a triangular distribution. This result indicates that the front-row anti-slide piles have sufficient rigidity and that the thrust of the back side of the landslide body is transmitted to the anchoring section of pile P1. The maximum dynamic earth pressure of pile P1 (55.6 kPa) is only 10.5% of the maximum value of pile P3 (529 kPa); that is, the thrust of the landslide becomes very small when transmitted to the front-row anti-slide piles.

Dynamic strain response

Dynamic strain with input PGA

Response dynamic strain refers to the seismic-action-induced strain experienced by the pile. The peak dynamic strain is the mean value of the positive and negative peaks of the dynamic strain-time curve. Figure 19 shows the relationship between the peak dynamic strain of the pile and the input acceleration

amplitude. The peak dynamic strain of the pile caused by an operating frequency of 3 Hz is greater than that caused by 10 Hz. In Fig. 19a, the dynamic strain of the back-row piles of bridge foundation P2 is distributed from 26–88 $\mu\epsilon$. When PGA is 0.5 g, the dynamic strain value of top point S7 of the bridge foundation reaches 176 $\mu\epsilon$, which is a significant increase of approximately 2.7 times the value when PGA is 0.4 g. When PGA = 0.5 g, the landslide slides, causing the thrust of the sliding body to increase sharply. At the same time, the PGA amplification effect of the slope surface causes the top section of the pile to carry more dynamic stress, resulting in a sudden increase in pile strain. The maximum dynamic strain is transferred from the top to the bottom of the pile. When PGA > 0.5 g, the dynamic strain at point S7 decreases sharply, while the dynamic strains at the adjacent points S8 and S9 increase. This result indicates that under the action of ground motion, the deformation of the bridge foundation first occurs on the upper part of the pile. When the pile is subjected to the critical acceleration amplitude of PGA = 0.5 g, the middle and lower parts of the pile share the excess seismic loading. The overall bearing capacity of the bridge foundation can be optimally utilized. In Fig. 19b, the maximum dynamic strain of the front-row piles of bridge foundation P2 appears at point S14 on the sliding surface, with a maximum value of 207 $\mu\epsilon$. The evolution characteristics of the dynamic strain can be divided into three stages: slowly increasing (PGA < 0.4 g), rapid growth (PGA = 0.4–0.6 g), stable (PGA \geq 0.6 g).

Dynamic strain distribution with pile depth

Figure 20 shows the distribution of the peak dynamic strain of the pile with pile depth. As shown in Fig. 20a, the dynamic strain peaks of the back-row anti-slide pile P3 are triangular in the section with points S1–S4 and square in the section with points S4–S6. The maximum strain appears in the breccia layer (S4). When PGA = 0.5 g, the increase in the amplitude of the dynamic strain is maximized. The

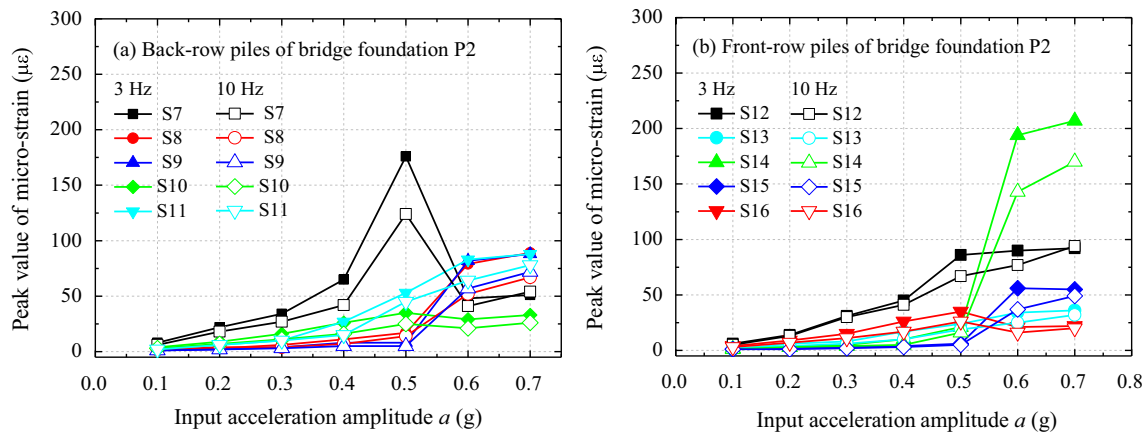


Fig. 19 a, b The relationships between the peak dynamic strain of bridge pile foundation P2 and the input acceleration amplitude

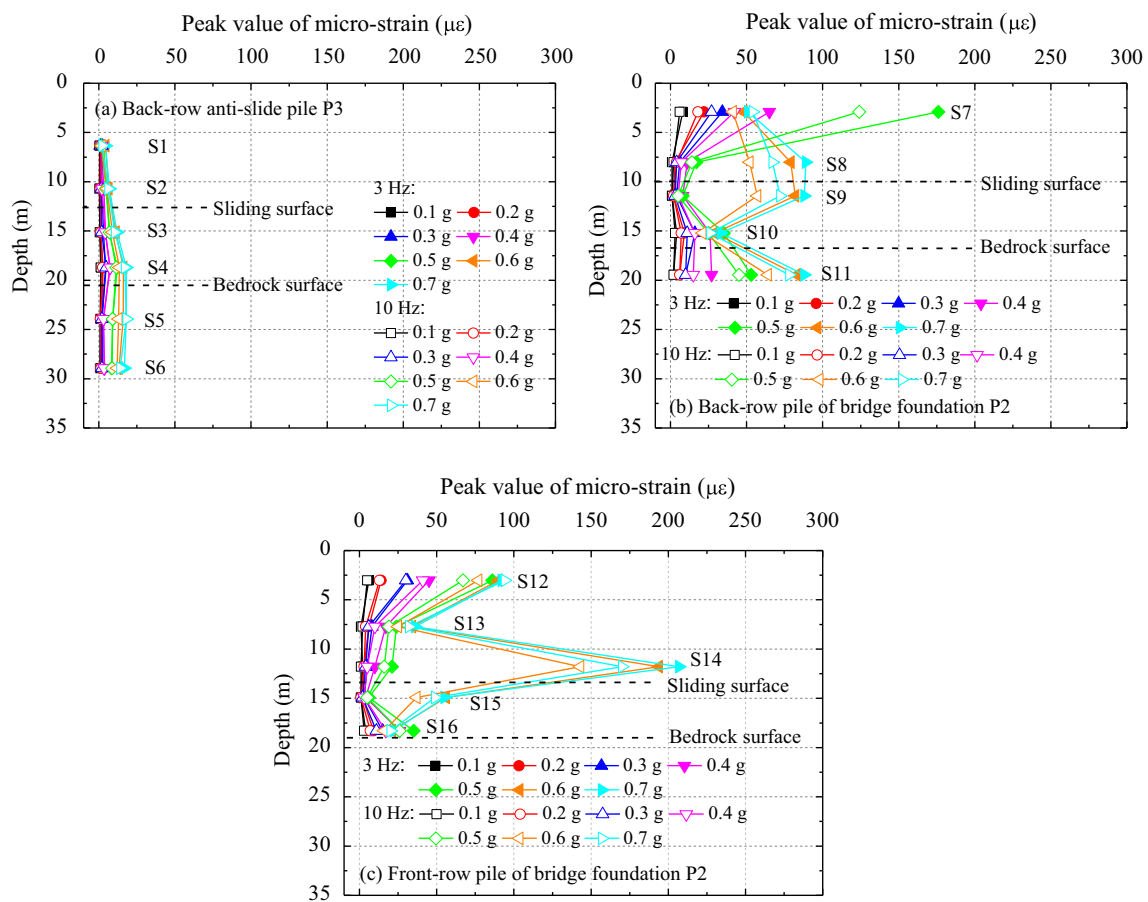


Fig. 20 The peak dynamic strain of the pile distributed along the pile for a PGA of 0.1–0.7 g. **a** Back-row anti-slide pile P3. **b** Back-row pile of bridge foundation P2. **c** Front-row pile of bridge foundation P2

dynamic strain of pile P3 is very small, with a maximum dynamic strain of only 18.0 $\mu\epsilon$ when PGA = 0.7 g. Pile P3 has sufficient flexural rigidity and can effectively resist the deformation caused by the slope slip. The dynamic strain of the front-row anti-slide pile P1 is the smallest, with a maximum dynamic strain of only 11.0 $\mu\epsilon$. The other small strain distributions of piles P2 and P3 are not provided here.

When the input PGA is less than or equal to 0.5 g, the dynamic strain in the back-row piles of the bridge foundation P2 decreases from the slope surface to the landslip surface and then increases to the bedrock surface in a bow shape, as shown in Fig. 20b. The minimum dynamic strain occurs near the landslip surface. The breccia layer and the bedrock layer play restraining roles in the anchoring section of the bridge foundation. The micro-strain of pile P2 is small and is approximately 2–27 $\mu\epsilon$. When PGA = 0.6–0.7 g, the interaction between the pier and pile P3 is enhanced, the breccia layer is squeezed, and the maximum dynamic strain moves down to the landslip surface (point S9). The section of the bridge foundation embedded in the bedrock has a great constraint on the deformation of the upper pile, with a dynamic strain close to the maximum value at the slip surface (S11).

As shown in Fig. 20c, when the input PGA is less than or equal to 0.5 g, the strain distribution of the front-row piles of the bridge foundation P2 is similar to that of its back-row piles, resulting in a bow-shaped distribution. The dynamic strain of the pile above the slip surface decreases with increasing pile depth, and the minimum value can be found near the landslip surface (S15). The dynamic strain in the fine breccia layer increases with pile depth. When PGA = 0.6–0.7 g, the dynamic strain increases sharply with increasing PGA. The position of the maximum dynamic strain is transferred from the pile top to the landslip surface. Influenced by the resistance of the soil around the pile, the pile strain decreases progressively from the sliding surface to both sides of the sliding surface, showing a convex shape. The reason for this evolution of the pile strain from a bow shape to a convex shape is that the initial seismic load is low; hence, the landslide is weakly subjected to the PGA, but as the landslide thrust is released when the PGA increases, the bridge pile is subjected to greater seismic inertial force and landslide thrust from the upper pier, and the position of the maximum dynamic strain is shifted down to resist the landslide sliding.

When the input PGA is greater than 0.5 g, the dynamic strain distribution characteristics in the front-row and back-

row piles of the bridge foundation P2 change accordingly, indicating a synchronous force development of the pile foundation. The anti-seismic performance of the front-row anti-slide pile P1 is limited. The strong ground motion can change the dynamic stress distribution of the bridge foundation near the sliding surface, and the reinforcement range of the pile should increase. In a deposit slope strengthened by anti-slide piles, this effect may be the main reason why cracking or even breaking of the piles of the bridge foundation would occur near the sliding surface during earthquakes. Therefore, in the anti-seismic reinforcement design of the bridge foundation in landslides, the strain distribution characteristics of the piles should be considered.

Conclusions

Shaking table tests of a double-row anti-slide pile-reinforced bridge foundation in a landslide with a 1:40 similitude ratio were completed. Different ground motion intensities were input to investigate the seismic responses of the bridge foundation and to analyze the PGA amplification factors of the slope. The distribution of the landslide thrust and the pile strain were explored, after which the seismic performance of the design of the anti-slide pile-reinforced bridge foundation was verified. Ultimately, seismic design involving the use of an anti-slide pile-reinforced bridge foundation in a landslide in the Chenglan HSR was proven to be safe and reliable. The conclusions are summarized as follows:

- (1). The acceleration amplification effect of the bridge foundation and landslide under the action of an earthquake shows a “surface effect”, an “elevation effect”, and a “geological structure effect”. For a geological structure with soft top and hard bottom layers, the seismic response of a loose deposit layer is greater than that of the bedrock. As the input PGA increases, the PGA amplification factor of the slope first decreases and then increases rapidly.
- (2). For the reinforcement of the bridge foundation in the sliding section with front- and back-row anti-slide piles, the spacing between the back-row anti-slide piles and the bridge foundation is small, and the bridge cap and its adjacent slope maintain a large PGA amplification factor. Therefore, the acceleration response of the bridge foundation is enhanced, which is not conducive to the stability of the bridge foundation.
- (3). The force of the landslide thrust behind the piles is mainly carried by the upper part of the back-row anti-slide piles. The distribution of the landslide thrust changes from the shape of a spoon to the shape of a bow with increasing PGA. The resultant force action point in the pile body bearing the dynamic earth pressure shifts to the pile top with increasing input PGA, which is a result of the amplification effect of seismic waves and the redistribution of the pile-soil stress caused by the “arching effect”.
- (4). For medium- to low-intensity earthquakes ($PGA \leq 0.5 g$) (GB18306-2001), the peak dynamic strain of the bridge foundation appears at the pile top and gradually decreases with pile depth. For high-intensity earthquakes ($PGA > 0.5 g$), the maximum dynamic strain of the bridge foundation appears near the sliding surface, which is the main cause of the cracks and broken piles in bridge foundations; thus, this condition is not favourable for engineering protection. The load-bearing section of the bridge pile foundation near the sliding surface needs to be strengthened.
- (5). The higher the seismic frequency is, the stronger the acceleration response and the larger the PGA amplification factor of the slope. Under the action of an earthquake, anti-slide piles can reinforce the landslide and mitigate the dynamic response of the bridge foundation, which optimally minimizes the dynamic earth pressure behind the piles near the bedrock. Reinforcement by anti-slide piles can limit the dynamic responses of the bridge and the landslide and weaken the seismic response of the slope.

Funding information This study has been financially supported by the National Natural Science Foundation of China (Grant No. 51808542, 41761144077), and the Youth Innovation Promotion Association CAS (Grant No. 2019364).

References

- Al-Defae AH, Knappett JA (2014) Centrifuge modeling of the seismic performance of pile-reinforced slopes. *J Geotech Geoenviron* 140(6):04014014. [https://doi.org/10.1061/\(ASCE\)Gt.1943-5606.0001105](https://doi.org/10.1061/(ASCE)Gt.1943-5606.0001105)
- Anderson DG, Martin GR, Lam I, Wang JN (2009) Seismic analysis and design of retaining walls, buried structures, slopes, and embankments. National Cooperative Highway Research Program (NCHRP) Report 611. Transportation Research Board.
- Brara A, Klepaczko JR (2007) Fracture energy of concrete at high loading rates in tension. *Int J Impact Eng* 34(3):424–435. <https://doi.org/10.1016/j.ijimpeng.2005.10.004>
- Brennan AJ, Madabhushi SPG (2009) Amplification of seismic accelerations at slope crests. *Can Geotech J* 46(5):585–594. <https://doi.org/10.1139/T09-006>
- Brennan AJ, Thusyanthan NI, Madabhushi SP (2005) Evaluation of shear modulus and damping in dynamic centrifuge tests. *J Geotech Geoenviron* 131(12):1488–1497. [https://doi.org/10.1061/\(ASCE\)1090-0241\(2005\)131:12\(1488\)](https://doi.org/10.1061/(ASCE)1090-0241(2005)131:12(1488))
- Chigira M, Wu XY, Inokuchi T, Wang GH (2010) Landslides induced by the 2008 Wenchuan earthquake, Sichuan, China. *Geomorphology* 118(3-4):225–238. <https://doi.org/10.1016/j.geomorph.2010.01.003>
- Chotesuwan A, Mutsuyoshi H, Maki T (2012) Seismic behavior of bridges with pier and foundation strengthening: PsD tests and analytical

- study. *Earthq Eng Struct D* 41(2):279–294. <https://doi.org/10.1002/eqe.1129>
- Cui P, Zhu YY, Han YS, Chen XQ, Zhuang JQ (2009) The 12 May Wenchuan earthquake-induced landslide lakes: distribution and preliminary risk evaluation. *Landslides* 6(3):209–223. <https://doi.org/10.1007/s10346-009-0160-9>
- Du Y, Yuan C, Wang Y, Tao Y-J (2012) Major geological hazard and geological alignment of Chengdu-Lanzhou railway. *J Railway Eng Soc* 8:11–15 (in Chinese)
- Ellis EA, Durrani IK, Reddish DJ (2010) Numerical modelling of discrete pile rows for slope stability and generic guidance for design. *Geotechnique* 60(3):185–195. <https://doi.org/10.1680/geot.7.00090>
- Fang YS, Chen TJ, Holtz RD, Lee WF (2003) Reduction of boundary friction in model tests. *Geotech Test J* 27(1):3–12 <https://doi.org/10.1520/GTJ10812>
- GB18306-2001 (2001) Seismic ground motion parameter zonation map of China.
- Gorum T, Fan XM, van Westen CJ, Huang RQ, Xu Q, Tang C, Wang GH (2011) Distribution pattern of earthquake-induced landslides triggered by the 12 May 2008 Wenchuan earthquake. *Geomorphology* 133(3–4):152–167. <https://doi.org/10.1016/j.geomorph.2010.12.030>
- Haeri SM, Kavand A, Rahmani I, Torabi H (2012) Response of a group of piles to liquefaction-induced lateral spreading by large scale shake table testing. *Soil Dyn Earthq Eng* 38:25–45. <https://doi.org/10.1016/j.soildyn.2012.02.002>
- Han Q, Du XL, Liu JB, Li ZX, Li LY, Zhao JF (2009) Seismic damage of highway bridges during the 2008 Wenchuan earthquake. *Earthq Eng Vib* 8(2):263–273. <https://doi.org/10.1007/s11803-009-8162-0>
- Hashash YM, Dashti S, Romero MI, Ghayoomi M, Musgrove M (2015) Evaluation of 1-D seismic site response modeling of sand using centrifuge experiments. *Soil Dyn Earthq Eng* 78:19–31. <https://doi.org/10.1016/j.soildyn.2015.07.003>
- Hashash YM, Park D (2002) Viscous damping formulation and high frequency motion propagation in non-linear site response analysis. *Soil Dyn Earthq Eng* 22(7):611–624. [https://doi.org/10.1016/S0267-7261\(02\)00042-8](https://doi.org/10.1016/S0267-7261(02)00042-8)
- Hobiger M, Wegler U, Shiomi K, Nakahara H (2012) Coseismic and postseismic elastic wave velocity variations caused by the 2008 Iwate-Miyagi Nairiku earthquake, Japan. *J Geophys Res-Sol Earth* 117(B9). <https://doi.org/10.1029/2012JB009402>
- Huang F, Li M, Ma Y, Han Y, Tian L, Yan W, Li X (2017) Studies on earthquake precursors in China: a review for recent 50 years. *Geodesy Geodyn* 8(1):1–12. <https://doi.org/10.1016/j.geog.2016.12.002>
- Huang RQ, Li YR, Qu K, Wang K (2013) Engineering geological assessment for route selection of railway line in geologically active area: a case study in China. *J Mt Sci-Engl* 10(4):495–508. <https://doi.org/10.1007/s11629-013-2660-2>
- Hubbard J, Shaw JH (2009) Uplift of the Longmen Shan and Tibetan plateau, and the 2008 Wenchuan (M=7.9) earthquake. *Nature* 458(7235):194–197. <https://doi.org/10.1038/nature07837>
- Hwang H, Jernigan JB, Lin YW (2000) Evaluation of seismic damage to Memphis bridges and highway systems. *J Bridg Eng* 5(4):322–330. [https://doi.org/10.1061/\(ASCE\)1084-0702\(2000\)5:4\(322\)](https://doi.org/10.1061/(ASCE)1084-0702(2000)5:4(322))
- Iai S (1989) Similitude for shaking table tests on soil-structure-fluid model in 1g gravitational field. *Soils Found* 29(1):105–118. <https://doi.org/10.3208/sandf1972.29.105>
- JGJ94-2008 (2008) Technical code for building pile foundations. China Architecture and Building Press, Beijing
- Kanagasabai S, Smethurst JA, Powrie W (2011) Three-dimensional numerical modelling of discrete piles used to stabilize landslides. *Can Geotech J* 48(9):1393–1411. <https://doi.org/10.1139/T11-046>
- Kobayashi H, Tamura K, Tanimoto S (2002) Hybrid vibration experiments with a bridge foundation system model. *Soil Dyn Earthq Eng* 22(9–12):1135–1141. [https://doi.org/10.1016/S0267-7261\(02\)00140-9](https://doi.org/10.1016/S0267-7261(02)00140-9)
- Kowalsky MJ (2000) Deformation limit states for circular reinforced concrete bridge columns. *J Struct Eng-Asce* 126(8):869–878. [https://doi.org/10.1061/\(ASCE\)0733-9445\(2000\)126:8\(869\)](https://doi.org/10.1061/(ASCE)0733-9445(2000)126:8(869))
- Lee DH, Choi E, Zi G (2005) Evaluation of earthquake deformation and performance for RC bridge piers. *Eng Struct* 27(10):1451–1464. <https://doi.org/10.1016/j.engstruct.2005.04.009>
- Li JZ, Yan JK, Peng TB, Han L (2014) Shake table studies of seismic structural systems of a Taizhou Changjiang highway bridge model. *J Bridg Eng* 20(3):04014065. [https://doi.org/10.1061/\(ASCE\)BE.1943-5592.0000650](https://doi.org/10.1061/(ASCE)BE.1943-5592.0000650)
- Li JZ, Peng TB, Xu Y (2008) Damage investigation of girder bridges under the Wenchuan earthquake and corresponding seismic design recommendations. *Earthq Eng Vib* 7(4):337–344. <https://doi.org/10.1007/s11803-008-1005-6>
- Li LQ, Ju NP, Zhang S, Deng XX, Sheng DC (2019) Seismic wave propagation characteristic and its effects on the failure of steep jointed anti-dip rock slope. *Landslides* 16:105–123. <https://doi.org/10.1007/s10346-018-1071-4>
- Lin CH, Li HH, Weng MC (2018) Discrete element simulation of the dynamic response of a dip slope under shaking table tests. *Eng Geol* 243:168–180. <https://doi.org/10.1016/j.enggeo.2018.07.005>
- Lin ML, Wang KL (2006) Seismic slope behavior in a large-scale shaking table model test. *Eng Geol* 86(2–3):118–133. <https://doi.org/10.1016/j.enggeo.2006.02.011>
- Lirer S (2012) Landslide stabilizing piles: experimental evidences and numerical interpretation. *Eng Geol* 149:70–77. <https://doi.org/10.1016/j.enggeo.2012.08.002>
- Liu J, Liu FH, Kong XJ, Yu L (2016) Large-scale shaking table model tests on seismically induced failure of concrete-faced rockfill dams. *Soil Dyn Earthq Eng* 82:11–23. <https://doi.org/10.1016/j.soildyn.2015.11.009>
- Ma N, Wu HG, Ma HM, Wu XY, Wang GH (2019) Examining dynamic soil pressures and the effectiveness of different pile structures inside reinforced slopes using shaking table tests. *Soil Dyn Earthq Eng* 116:293–303. <https://doi.org/10.1016/j.soildyn.2018.10.005>
- Medel-Vera C, Ji TJ (2016) A stochastic ground motion accelerogram model for Northwest Europe. *Soil Dyn Earthq Eng* 82:170–195. <https://doi.org/10.1016/j.soildyn.2015.12.012>
- Nian TK, Jiang JC, Wang FW, Yang Q, Luan MT (2016) Seismic stability analysis of slope reinforced with a row of piles. *Soil Dyn Earthq Eng* 84:83–93. <https://doi.org/10.1016/j.soildyn.2016.01.023>
- Pal S, Kaynia AM, Bhasin RK, Paul DK (2012) Earthquake stability analysis of rock slopes: a case study. *Rock Mech Rock Eng* 45(2):205–215. <https://doi.org/10.1007/s00603-011-0145-6>
- Pastor M, Haddad B, Sorbino G, Cuomo S, Drempetic V (2009) A depth-integrated, coupled SPH model for flow-like landslides and related phenomena. *Int J Numer Anal Met* 33(2):143–172. <https://doi.org/10.1002/nag.705>
- Rong MS, Wang ZM, Woolery EW, Lyu YJ, Li XJ, Li SY (2016) Nonlinear site response from the strong ground-motion recordings in western China. *Soil Dyn Earthq Eng* 82:99–110. <https://doi.org/10.1016/j.soildyn.2015.12.001>
- Roten D, Föh D, Bonilla LF (2013) High-frequency ground motion amplification during the 2011 Tohoku earthquake explained by soil dilatancy. *Geophys J Int* 193(2):898–904. <https://doi.org/10.1093/gji/ggt001>
- Shi ZM, Wang YQ, Peng M, Chen JF, Yuan J (2015) Characteristics of the landslide dams induced by the 2008 Wenchuan earthquake and dynamic behavior analysis using large-scale shaking table tests. *Eng Geol* 194:25–37. <https://doi.org/10.1016/j.enggeo.2014.10.009>
- Srilatha N, Latha GM, Puttappa CG (2013) Effect of frequency on seismic response of reinforced soil slopes in shaking table tests. *Geotext Geomembr* 36:27–32. <https://doi.org/10.1016/j.geotextmem.2012.10.004>

- Sun H, Niu FJ, Zhang KJ, Ge XR (2017) Seismic behaviors of soil slope in permafrost regions using a large-scale shaking table. *Landslides* 14(4):1513–1520. <https://doi.org/10.1007/s10346-017-0823-x>
- Sun ZL, Kong LW, Guo AG, Tian H (2015) Effects of stress ratio and moisture condition of loose deposits on their dynamic parameters and ground response spectrum. *Rock Soil Mech* 36(10):2765–2772. <https://doi.org/10.16285/j.rsm.2015.10.004> (in Chinese)
- Tang L, Ling XZ, Xu PJ, Gao X, Wang DS (2010) Shake table test of soil-pile groups-bridge structure interaction in liquefiable ground. *Earthq Eng Vib* 9(1):39–50. <https://doi.org/10.1007/s11803-009-8131-7>
- TB10002.5-2005 (2005) Code for design on subsoil and foundation of railway bridge and culvert. China Railway Press, Beijing, pp 25–102
- Toritsu SS, Sato J, Towhata I, Honda T (2010) 1-G model tests and hollow cylindrical torsional shear experiments on seismic residual displacements of fill dams from the viewpoint of seismic performance-based design. *Soil Dyn Earthq Eng* 30(6):423–437. <https://doi.org/10.1016/j.soildyn.2009.12.016>
- Wang FW, Cheng QG, Highland L, Miyajima M, Wang HB, Yan CG (2009) Preliminary investigation of some large landslides triggered by the 2008 Wenchuan earthquake, Sichuan Province, China. *Landslides* 6(1):47–54. <https://doi.org/10.1007/s10346-009-0141-z>
- Wang KL, Lin ML (2011) Initiation and displacement of landslide induced by earthquake—a study of shaking table model slope test. *Eng Geol* 122(1-2):106–114. <https://doi.org/10.1016/j.enggeo.2011.04.008>
- Wasowski J, Keefer DK, Lee CT (2011) Toward the next generation of research on earthquake-induced landslides: current issues and future challenges. *Eng Geol* 122(1-2):1–8. <https://doi.org/10.1016/j.enggeo.2011.06.001>
- Xu G, Yao L, Gao Z, Li Z (2008) Large-scale shaking table model test study on dynamic characteristics and dynamic responses of slope. *Chin J Rock Mech Eng* 27(3):624–632 (in Chinese)
- Xu Q, Fan XM, Huang RQ, Van Westen C (2009) Landslide dams triggered by the Wenchuan Earthquake, Sichuan Province, south west China. *B Eng Geol Environ* 68(3):373–386. <https://doi.org/10.1007/s10064-009-0214-1>
- Xu Q, Liu H, Zou W, Fan X, Chen J (2010) Large-scale shaking table test study of acceleration dynamic responses characteristics of slopes. *Chin Chin J Rock Mech Eng* 29(12):2420–2428 (in Chinese)
- Yin YP, Li B, Wang WP (2015) Dynamic analysis of the stabilized Wangjiayan landslide in the Wenchuan Ms 8.0 earthquake and aftershocks. *Landslides* 12(3):537–547. <https://doi.org/10.1007/s10346-014-0497-6>
- Yu YZ, Deng LJ, Sun X, Lu H (2010) Centrifuge modeling of dynamic behavior of pile-reinforced slopes during earthquakes. *J Cent South Univ T* 17(5):1070–1078. <https://doi.org/10.1007/s11771-010-0599-9>
- Yuan LJ, Liu XS, Wang XG, Yang YS, Yang ZQ (2014) Seismic performance of earth-core and concrete-faced rock-fill dams by large-scale shaking table tests. *Soil Dyn Earthq Eng* 56:1–12. <https://doi.org/10.1016/j.soildyn.2013.09.019>
- Zhang JQ, Qu HL, Liao Y, Ma YX (2012) Seismic damage of earth structures of road engineering in the 2008 Wenchuan earthquake. *Environ Earth Sci* 65(4):987–993. <https://doi.org/10.1007/s12665-011-1519-5>
- Zhang ZL, Wang T, Wu SR, Tang HM, Liang CY (2017) Investigation of dormant landslides in earthquake conditions using a physical model. *Landslides* 14(3):1181–1193. <https://doi.org/10.1007/s10346-017-0813-z>